Open Access

Journal of Energy and Power Technology

Research Article

Interconnected Operations of Electric Vehicle to Grid and Microgrid

Ganisetti Vijay Kumar, Min-Ze Lu, Chang-Ming Liaw *

Department of Electrical Engineering, National Tsing Hua University, Hsinchu, Taiwan, ROC; E-Mails: vijaykumarganisetti@gmail.com; b10112016@gmail.com; cmliaw@ee.nthu.edu.tw

* **Correspondence:** Chang-Ming Liaw; E-Mail: cmliaw@ee.nthu.edu.tw

Academic Editor: Aritra Ghosh

Special Issue: Progress of Wind Energy Technology and Its Maintenance

Journal of Energy and Power Technology
2021, volume 3, issue 2
doi:10.21926/jept.2102023

Received: December 19, 2020
Accepted: May 13, 2021
Published: May 31, 2021

Abstract

This paper presents the development of a high-performance electric vehicle (EV) synchronous reluctance motor (SynRM) drive and its vehicle-to-grid (V2G) and vehicle-to-microgrid (V2M) bidirectional operations. The EV motor drive boostable DC-link voltage is established by a battery through a bilateral interface boost-buck DC-DC converter for good driving performance over a wide speed range. The motor efficiency is 92.3% near the rated load. In idle conditions, the embedded interface converter and inverter of the motor drive can be arranged to perform the G2V/V2G operations by adding external LC low-pass filters. The on-board battery can be charged from the mains in G2V mode with good line-drawn power quality. Alternatively, in V2G mode, the battery can send the preset power back to the utility grid with good current waveform quality. Besides, the same schematics can also conduct the M2V/V2M operations. A wind switched-reluctance generator (SRG) based microgrid is used as a test plant. The EV mobile energy storage application to microgrids is successfully offered through the arranged controls for effectively utilizing renewable sources. The measured results verify the normal operations with satisfactory performances for all power stages and operation cases.

Keywords

Electric vehicle; Synrm; G2V; V2G; V2M; M2V; wind generator; microgrid

1. Introduction

Compared to the induction motor and permanent-magnet synchronous motor (PMSM), a synchronous reluctance motor (SynRM) [1, 2] has a simpler rotor structure without permanent magnets and conductors, which makes it cogging torque-free and suitable for high-speed running. Hence, SynRM has potential applicability in EV driving [3–5]. However, the SynRM has higher current and torque ripples, higher core loss, and lower power factor due to the slotted laminated rotor. Among the main performance issues, proper commutation angle setting is the most crucial one. Some researchers also emphasize loss minimization control (LMC) [6–11]. Due to the slotted rotor, SynRM has inherently nonlinear inductance and higher ripple current [12]. Some studies [11, 13, 14] have been focused on advanced current controls, considering the varied motor parameters and nonlinear behaviors.

As explored earlier [15, 16], the EV drive equipped with a bidirectional interface converter providing boostable DC-link voltage from the battery can yield better performance. Among the existing bidirectional converters [17, 18], the one-leg boost-buck converter is the most popular for EV applications and is adopted here. In the established EV SynRM drive, the speed-dependent voltage command is set, and the rigid motor drive DC-link voltage with fast command tracking response is established by the developed control scheme. Excluding the interface converter, an earlier study [19] proposed optimized thermal management for Li-ion batteries that can avoid thermal runway leading to an explosion.

As generally recognized, the G2V/V2G operations [20–30] incorporated the EV with the utility grid to effectively reduce fossil energy utilization. In recent years, G2V/V2G operations are gradually attracted attention due to the increase in EV usage. A bidirectional on-board charger is needed to conduct the G2V/V2G operations. In the established EV drive, through proper arrangement and control, the embedded SynRM drive inverter can normally operate as a switch-mode rectifier (SMR) based charger in G2V mode and operate as a PWM inverter to conduct V2G discharging operations in both three-phase and single-phase conditions.

The incorporated operation of EV to microgrid with renewable sources can more effectively reduce fossil energy consumption and carbon-dioxide emission [26, 31–37]. The details on the effective utilization of renewable energies to EV charging can be referred elsewhere [33–35]. In the developed EV drive, the M2V/V2M bidirectional operations can also be conductible through the original schematics and the arranged controls. A prototype wind SRG based DC microgrid is used as the test plant for verification.

This paper presents EV SynRM drives with V2G/G2V and V2M/M2V operation controls. The power circuits and control schemes are aptly designed for the developed EV drive in both driving and idle operation modes. Besides, the measured results verify all operation performances, including the EV driving characteristics and the bidirectional EV interconnected operations to grid and microgrid.

2. System Configuration

In general, using renewable sources can reduce fossil energy consumption and consequently carbon dioxide emission. Microgrid and electric vehicles are the two example applications of

renewable sources. Combining microgrids, electric vehicles, and the energy storage system can more effectively reduce fossil energy consumption and carbon dioxide emission. Figure 1 shows the conceptual configuration of a DC microgrid incorporated with an electrical vehicle (EV), traditional grid, and specific battery energy storage system (BESS). All sources and energy storage devices are interfaced to the common DC bus through proper DC/DC or AC/DC converters. Typically, the bidirectional converters are employed in storage devices for conducting discharging/charging operations. The DC microgrid is connected to the utility grid using a bidirectional inverter through a proper synchronization process and control, which can perform the bidirectional microgrid-to-grid (M2G) and grid-to-microgrid (G2M) operations. With the electric vehicles with suitable interface converters, the grid-to-vehicle (G2V)/vehicle-to-grid (V2G) and microgrid-to-vehicle (M2V)/vehicle-to-microgrid (V2M) can also be conductible.

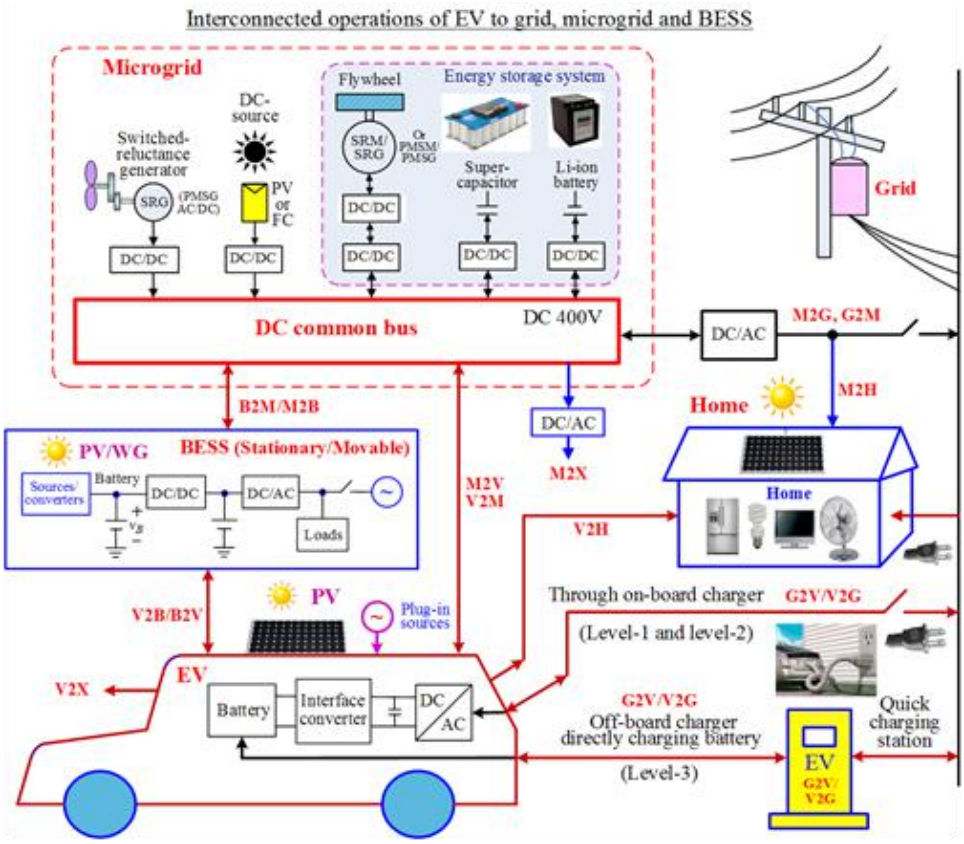

Figure 1 Conceptual configuration of microgrid incorporated with EV, grid, home, and BESS.

Figure 2 shows the configuration for the developed EV SynRM drive with bidirectional V2G/G2V and V2M/M2V functions. Figure 3 and Figure 4 depict the detailed schematics under three-phase and single-phase grid-connected cases. The motor drive contains a battery bank, a one-leg bidirectional boost-buck interface converter, an inverter-fed SynRM drive, a dynamic brake leg, a flywheel, and a load permanent-magnet synchronous generator. For enhancing the SynRM drive efficiencies over a wide speed range, a varied and boosted speed-dependent DC-link voltage is established from the battery through the bidirectional interface converter. Figure 5 and Figure 6 depict the control schemes of the SynRM drive and the battery interface converter in the driving mode.

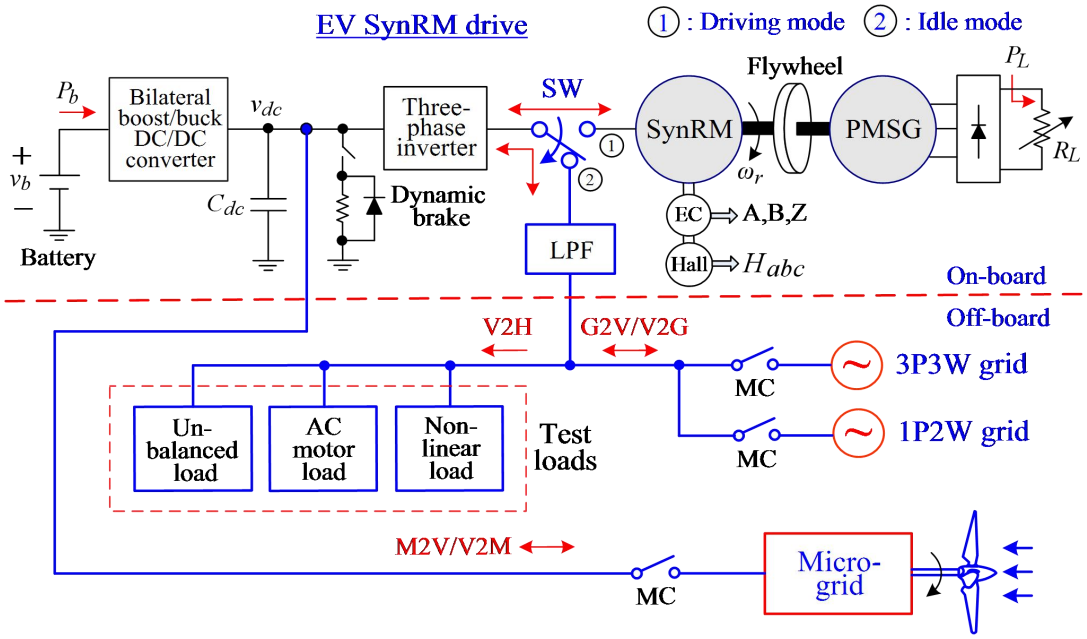

Figure 2 System configuration of the established EV SynRM drive with bidirectional V2G/G2V and V2M/M2V functions.

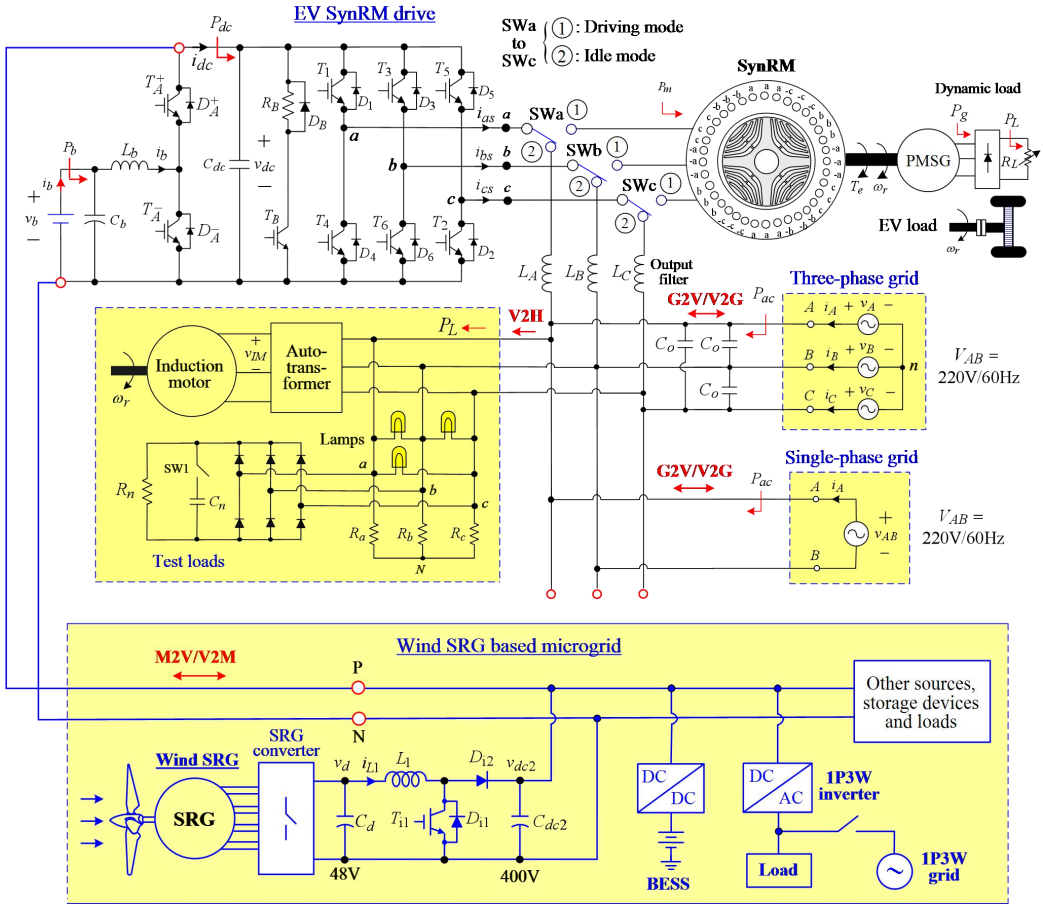

Figure 3 Schematic of the established EV SynRM drives with bidirectional V2G/G2V and V2M/M2V functions.

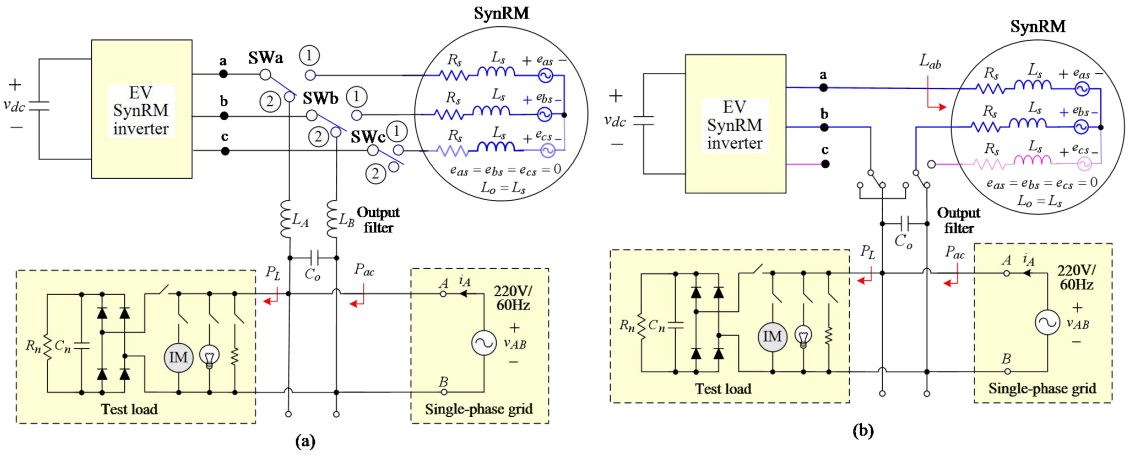

Figure 4 Schematics of the established EV SynRM drive with bidirectional V2G/G2V functions to single-phase grid: (a) using external inductor; (b) using integrated inductor of armature winding.

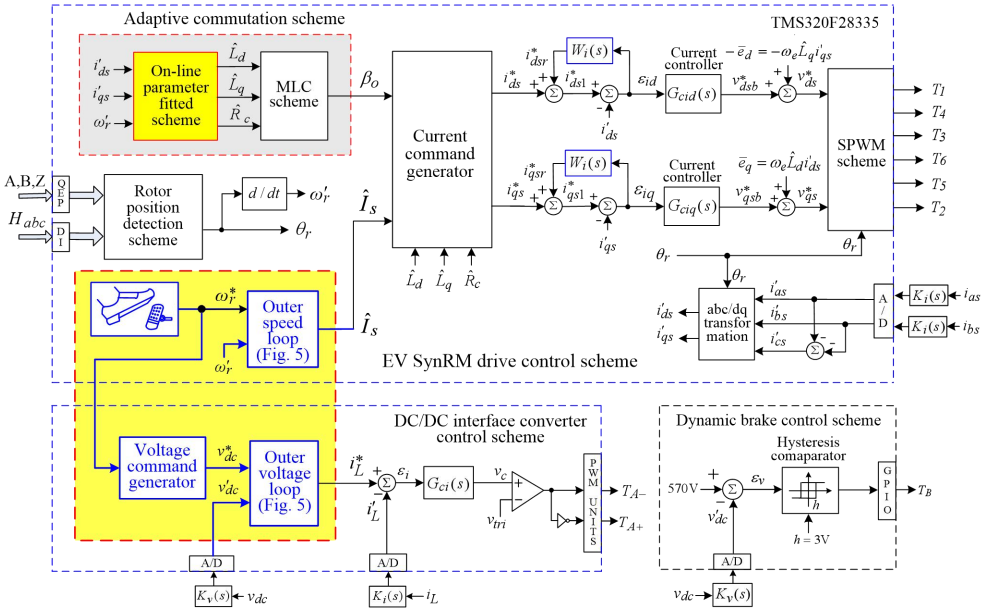

Figure 5 Control scheme of the established EV SynRM drive in driving mode.

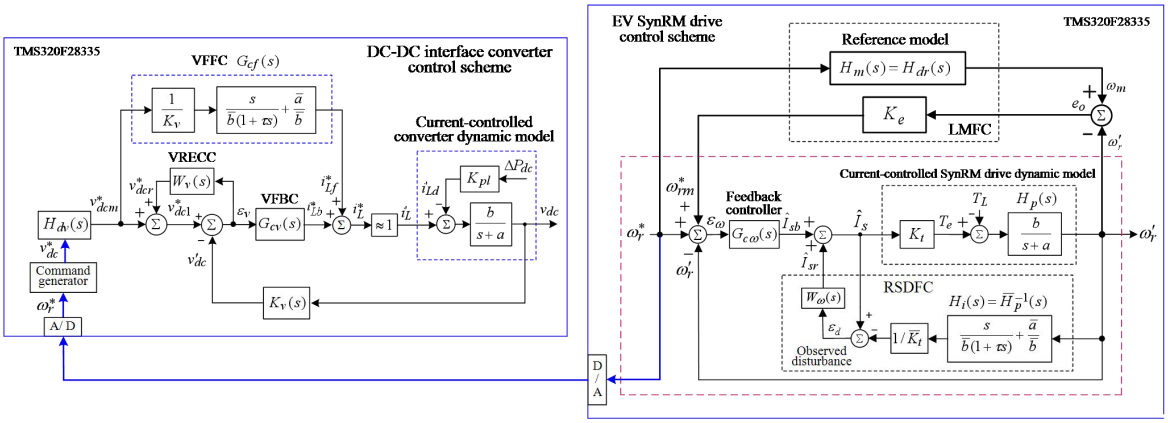

Figure 6 Outer-loop control schemes of the EV SynRM drive and the interface converter.

The external LC low-pass filters are added to achieve the G2V/V2G operations under idle mode. Figure 7(a) and (b) show the control schemes of these two modes. In V2M operation, the microgrid battery or inverter-fed home appliances can be supported by energy from the EV. Conversely, in M2V mode, the EV battery auxiliary charging can be done through the microgrid. Moreover, the M2G/G2M is also applied through the same schematics. The control scheme of the EV battery interface converter is identical to Figure 7(b), while the microgrid-related power circuits and control schemes are presented later in Sec. 7.

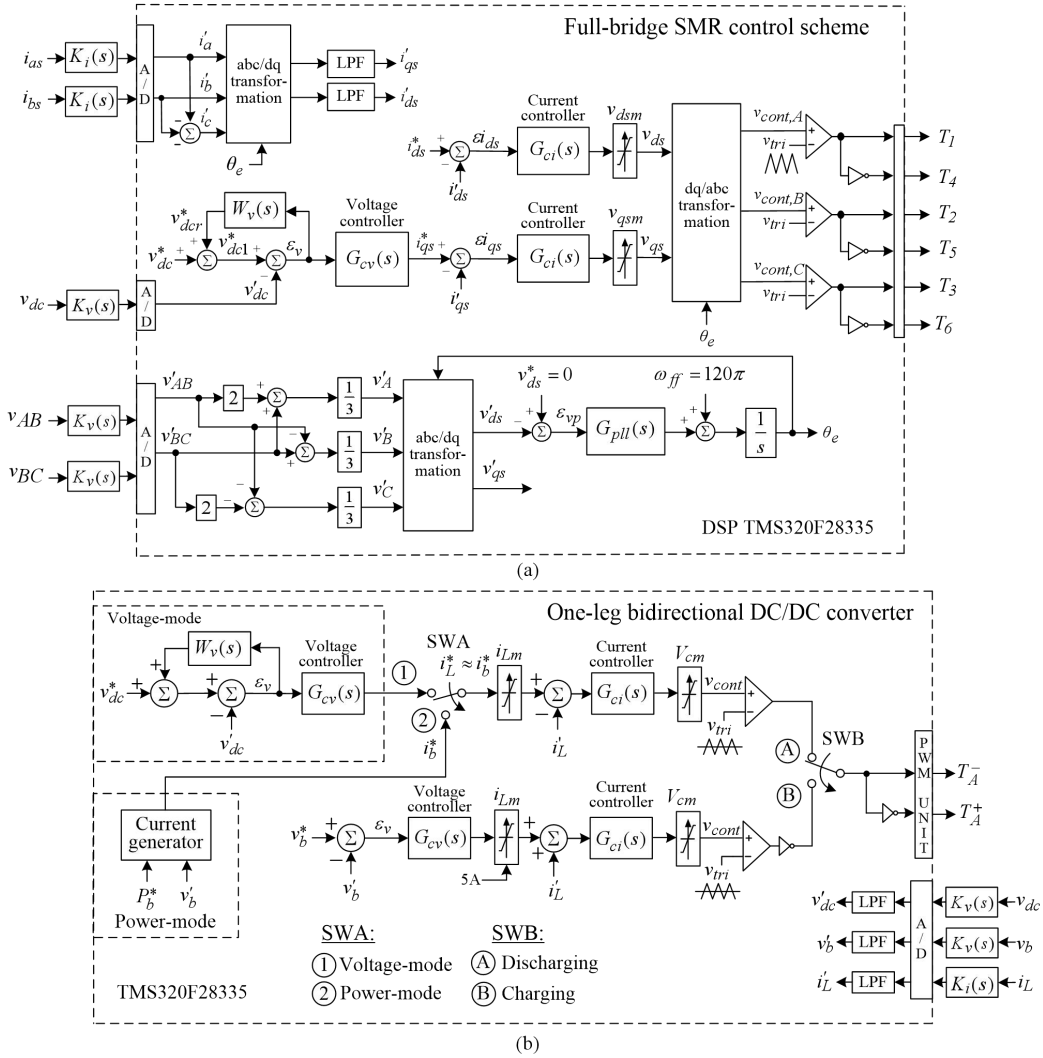

Figure 7 Control schemes of the established G2V/V2G functions in idle mode: (a) SMR; (b) one-leg interface converter.

3. EV Synchronous Reluctance Motor Drive

3.1 System Components

A brief summary of the components of the established SynRM drive is as follows:

(1) SynRM: Three-phase, 4-pole, 3.7 kW, 2000rpm.

(2) SynRM PWM inverter: Constructed using three single-leg IGBT modules FF50R12RT4.

(3) Position sensing devices: Incremental encoder (A, B, Z) (2500 pulses/rev) and three-phase Hall sensors.

(4) Load SPMSG: Three-phase, 8-pole, 5 kW, 2000rpm.

(5) Flywheel: $J = 0.048355\ \text{kg} \cdot \text{m}^2$.

(6) Dynamic brake: The brake resistance is $R_B = 30\Omega/1000\text{W}$. The voltage command of 570V is set, and the bang-bang control with a hysteresis band of *h* =3V is made.

3.2 Governing Equations

The voltage equations of a SynRM in rotor reference frame can be derived as [2]:

$$v_{qs} = \left(R_s + L_q \frac{d}{dt}\right) i_{qs} + e_q, e_q \equiv \omega_r L_d i_{ds} \#(1)$$

$$v_{ds} = \left(R_s + L_d \frac{d}{dt}\right) i_{ds} + e_d, e_d \equiv -\omega_r L_q i_{qs} \#(2)$$

$$L_d = L_{ls} + L_{md} = L_{ls} + 3(L_A + L_B)/2 \#(3)$$

$$L_q = L_{ls} + L_{mq} = L_{ls} + 3(L_A - L_B)/2 \#(4)$$

Here L_d (L_q) is d-(q-) axis armature inductance, L_{md} (L_{mq}) is d-(q-) axis magnetizing inductance, and e_d (e_q) is the coupled d-(q-) axis back-EMF.

3.3 Equivalent Circuits

Figure 8 shows the d-and q-axis equivalent circuits considering iron loss (represented by R_c) [6, 11], which also depicts the terminal currents ($i_{qs} = i_{mq} + i_{cq}, i_{ds} = i_{md} + i_{cd}$) and the torque currents (i_{mq}, i_{md}).

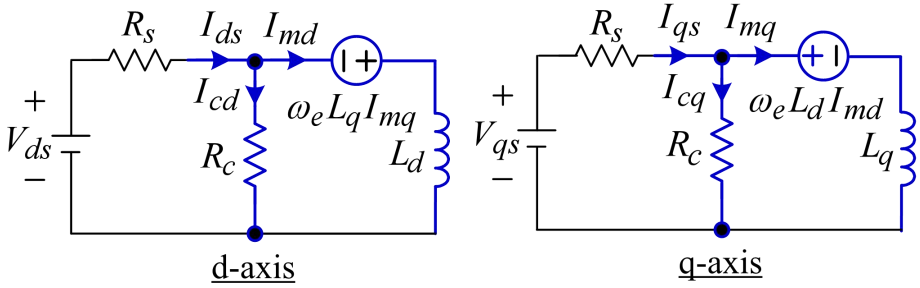

Figure 8 Equivalent circuits and phasors of SynRM.

The developed torque can be expressed using i_{mq} and i_{md} as,

$$T_e = \frac{3P}{4}(L_d - L_q) i_{mq} i_{md} = T_L + B\omega_r + J\frac{d\omega_r}{dt} \#(5)$$

Here *P* is the number of poles, T_L is the load torque, *B* is the total damping coefficient, and *J* is the total inertia constant.

By defining $\tilde{I}_{as} \equiv \hat{I}_s \angle \beta$ ($I_{ds} \equiv \hat{I}_s \cos\beta$, $I_{qs} \equiv \hat{I}_s \sin\beta$), and neglecting core loss, the commutation angle determined according to i_{qs} and i_{ds} is $\beta \equiv \beta_{o1} = 45^\circ$. However, the commutation angle β for yielding better performance will increase from $\beta_{o1} = 45^\circ$[11].

As explored theoretically and experimentally, the major SynRM parameters affecting the proper commutation angle setting, sequentially, are R_c, L_d, and L_q. The detailed estimation process for yielding the employed motor key parameters can be referred to in an earlier study [11]. The results are summarized below.

3.3.1 Winding Resistance

$R_s = 0.47\Omega$ using DC test.

3.3.2 D-and q-Axis Winding Inductances

The AC excitation method at 66.67Hz is applied at the directed d-axis and q-axis positions to measure the inductances under various current levels. The fitted incremental L_d and L_q are enlisted below:

$$\hat{L}_d(i_{ds}) = \begin{cases} 0.0766(\text{H}), i_{ds} \le 3\text{A} \\ d_1(i_{ds}) + d_2(\text{H}), i_{ds} > 3\text{A} \end{cases} \#(6)$$

Here $d_1 =$ -0.004 and $d_2 = 0.0886$.
And,

$$\hat{L}_q(i_{qs}) = \begin{cases} 0.0334(\text{H}), i_{qs} \le 0.6\text{A} \\ q_1 ln(i_{qs}) + q_2(\text{H}), 0.6\text{A} < i_{qs} \le 6\text{A} \\ 0.0113(\text{H}), i_{qs} > 6\text{A} \end{cases} \#(7)$$

$q_1 =$ -0.0096 and $q_2 = 0.0285$.

3.3.3 Core Loss Resistance

The measured core resistances are fitted with speed ω_r (in rpm) as,

$$\widehat{R}_c(\omega_r) = c_1(\omega_r) + c_2(\Omega), c_1 = 0.0255, c_2 = 34.719 \#(8)$$

3.4 Commutation Scheme

From Figure 7, the total loss P_t, including copper loss P_{cu} and core loss P_c, can be determined. Besides, the commutation angle β_o for minimizing P_t can be derived [6, 11].

$$\beta_o = \tan^{-1}\sqrt{\frac{\omega_e^2 L_d^2(R_s + R_c) + R_s R_c^2}{\omega_e^2 L_q^2(R_s + R_c) + R_s R_c^2}} \#(9)$$

The fitted ($\hat{L}_d$, $\hat{L}_q$, $\widehat{R}_c$) in equations (6) to (8) are used to determine the β_o angle online. The derivation of the q-and d-axis current commands for vector control can be obtained through the online determined angle β_o.

3.5 Dynamic Control Scheme

3.5.1 Current Control Scheme

Figure 5 shows the developed control scheme. The designed constituted controllers are listed below.

Feedback and Feedforward Controllers. The PI feedback controller is designed in the q-axis and is also suited for the d-axis controller. The designed controller considering the effect of slotting harmonics is based on an earlier study [11]:

$$G_{cid}(s) = G_{ciq}(s) = 5 + 50/s \#(10)$$

Based on (1) and (2), the feedback control signals v_{qsb}^* and v_{dsb}^* are augmented with the observed back-EMF feedforward control signals v_{qsf}^* and v_{dsf}^* to yield the PWM control signals:

$$v_{qs}^* = v_{qsb}^* + v_{qsf}^*, v_{qsf}^* = \bar{e}_q = \omega_e \hat{L}_d i_{ds}^{'} \#(11)$$

$$v_{ds}^* = v_{dsb}^* + v_{dsf}^*, v_{dsf}^* = -\bar{e}_d = -\omega_e \hat{L}_q i_{qs}^{'} \#(12)$$

Current Robust Error Cancellation Controller. To automatically enhance the current-tracking control performance and the robustness against the slotting effects, a current robust error cancellation controller (CRECC), as shown in Figure 5, is added. For instance, taking the q-axis current control scheme, a compensating current command i_{qsr}^* is added to the original command i_{qs}^* to yield the modified i_{qs1}^*. The robust weighting factor is as per an earlier study [11]:

$$W_i(s) = \frac{W_i}{1 + \tau_i s}, 0 \le W_i < 1 \#(13)$$

Here $W_i = 0.8$ and $\tau_i = 0.00318\text{s}$ are as per the compromised considerations in control performance and the ripple effects.

3.5.2 Speed Control Scheme

The right part of Figure 6 depicts the proposed robust speed model following the control scheme. It consists of a PI feedback controller, a robust speed observed disturbance feedforward controller (RSDFC), and a linear model following controller (LMFC). The designed controllers are enlisted below.

Feedback Controller. The basic PI controller is designed quantitatively at the chosen operating point ($\omega_r^{'} = 1900\text{rpm}, R_L = 33.9\Omega$) for the desired speed tracking response defined by $H_{dr}(s) = 2.647/(s + 2.627)$ as,

$$G_{c\omega}(s) = K_{P\omega} + \frac{K_{I\omega}}{s} = 2.5733 + \frac{1.1354}{s} \#(14)$$

RSDFC and LMFC. In the proposed RSDFC shown in Figure 6, an inverse nominal plant model $H_i(s) = \bar{H}_p^{-1}(s)$ is used to obtain the observed disturbance ε_d. The weighted current command $\hat{I}_{sr}$ yields the compensation control for the varied plant to preserve the desired tracking response as far as possible. As per the compromised considerations, the robust control weighting function $W_\omega(s) = W_\omega/(1 + \tau s) = 0.5/(1 + 0.001s)$ is set.

With the changing operating condition and system parameters, the model tracking error $e_o = \omega_m - \omega_r^{'}$ will exist under the imperfect control of RSDFC. To minimize the tracking error, the simple LMFC is applied. The reference model is set as $H_m(s) = H_{dr}(s)$. A compensated speed command $\omega_{rm}^* = K_e e_o$ ($K_e = 5$ is set here) is generated to yield the closer speed model following response.

Effectiveness Verification. Let the operating point be changed to ($\omega_r^{'} = 1900$rpm, $R_L = 16.67\Omega$). Figure 9 presents the plots of measured $\omega_r^{'}$ and $\hat{I}_s$ by various controllers. The normal operations can also yield results.

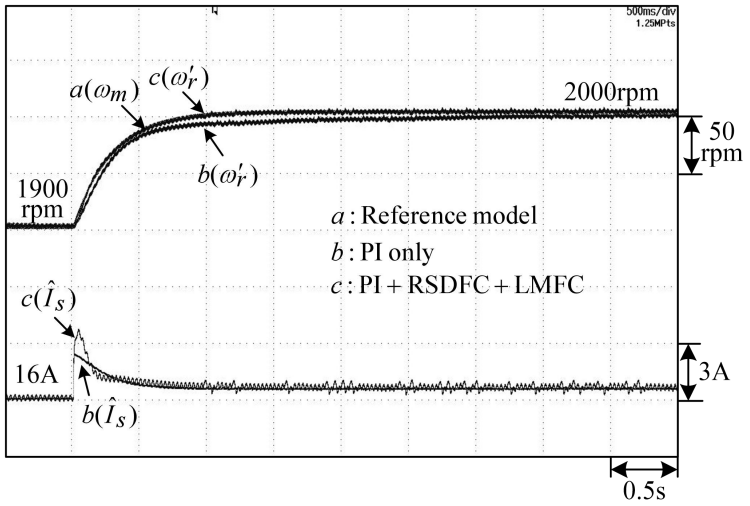

Figure 9 Measured $\omega_r^{'}$ and $\hat{I}_s$ of the developed SynRM drive due to a step speed command change ($\Delta\omega_r^* = 100$rpm) at ($V_{dc} = 550$V, $\omega_r^{'} = 1900$rpm, $R_L = 16.67\Omega$).

Figure 10 shows the measured $\omega_r^{'}$ and $\hat{I}_s$ as per the step load resistance change $R_L = 25\Omega \rightarrow 16.67\Omega$ at ($V_{dc} = 550$V, $\omega_r^{'} = 2000$rpm, $R_L = 25\Omega$). A significant improvement in load regulation response by the proposed RSDFC and LMFC can be observed.

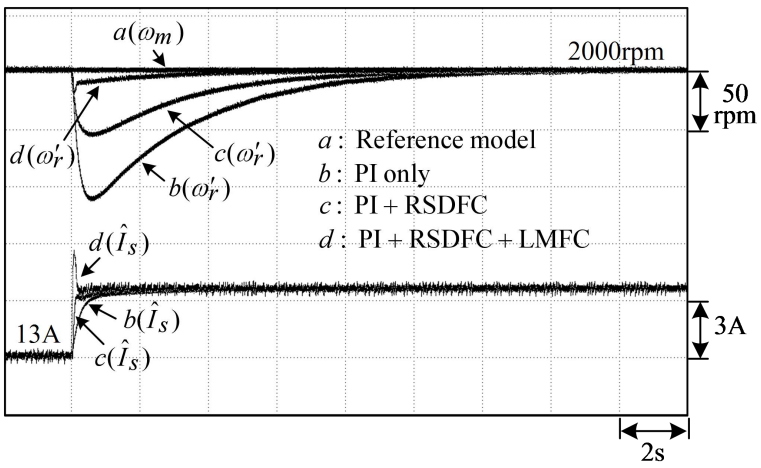

Figure 10 Measured $\omega_r^{'}$ and $\hat{I}_s$ of the developed SynRM drive due to a step load resistance change $R_L = 25\Omega \rightarrow 16.67\Omega$ at ($V_{dc} = 550$V, $\omega_r^{'} = 2000$rpm, $R_L = 25\Omega$).

4. Battery Interface Converter

4.1 Power Circuit

The system ratings and circuit components are:
(1) Rated voltages: battery: $V_b = 160$V, 18Ah, (LiFePo4) and DC-link voltage: $V_{dc} = 550$V.
(2) Power rating: $P_b = P_{dc} =$ 3.75 kW, $I_b = I_L = 23.44$A.
(3) Switching frequency: $f_s =$ 30 kHz.
(4) Energy storage inductor: $L_b = 1.5$ mH, the current ripples in both modes are identical to,

$$\Delta i_L = \frac{160 \times 0.7091}{1.5 \times 10^{-3} \times 30 \times 10^3} = 2.521\text{A}=0.108I_L$$

(5) Voltage filtering capacitors: $C_b = 1000$ μF/500V, $C_{dc} = 1100$ μF/800V.
(6) Power device: IGBT FF50R12RT4 (Infineon).

4.2 Control Scheme

As the battery interface converter mostly operates under boost mode for discharging, the designs of all controllers are conducted in this mode. Besides, it is also suitable for the buck converter mode. The design controllers are summarized below.

4.2.1 Current Controller

The current feedback controller is chosen to be PI type with,

$$G_{ci}(s) = K_{Pi} + \frac{K_{Ii}}{s} = 3 + \frac{10}{s} \#(15)$$

4.2.2 Voltage Control Scheme

After having a well-controlled current loop, $i_L^{'} \approx i_L^*$ is assumed. Thus, the voltage-loop dynamic behavior is represented by the control block depicted in the left part of Figure 6. The controller design methodologies include: (i) The feedback controller is quantitatively designed to meet the given regulation control specifications; (ii) The desired voltage tracking response, defined by a reference mode, is achieved by the voltage feedforward controller (VFFC) and the voltage robust error cancellation controller (VRECC). Besides, the regulation response can be further improved by the VRECC.

Voltage Feedback Controller (VFBC).

$$G_{cv}(s) = K_{Pv} + \frac{K_{vi}}{s} = 1.0556 + \frac{15.69}{s} \#(16)$$

VFFC and VRECC. According to the performance achievable by the designed converter, the desired voltage tracking response is defined by a reference model $H_{dv}(s)$ to generate the voltage reference response v_{dcm}^*.

$$H_{dv}(s) = \frac{r}{s+r} = \frac{66.67}{s+66.67} \#(17)$$

The VFFC is set as the inverse plant model using the estimated nominal model parameters ($\bar{a}$ and $\bar{b}$):

$$G_{cf}(s) = \frac{1}{K_v}\left(\frac{s}{\bar{b}(1+\tau s)} + \frac{\bar{a}}{\bar{b}}\right) \#(18)$$

$$\bar{a} = 11.3477, \bar{b} = 19444.15, K_{Pl} = 0.0000746 \#(19)$$

Here the pure differentiator s is replaced by a low-pass filter based alternative $s/(1+\tau s)$ with $\tau = 5 \times 10^{-5}$ to solve its practical unrealizable problem.

The robust weighting function is set as,

$$W_v(s) = \frac{W_v}{1+\tau_v s}, 0 \le W_v < 1 \#(20)$$

As per the compromised considerations, $W_v = 0.8$ and $\tau_v = 3.18 \times 10^{-5} s$ are selected here.

Let the operating point be $(V_{dc} = 500\text{V}, R_{dc} = 100\Omega)$, Figure 11 shows the measured $v_{dc}^{'}$ and i_L^* of the boost converter due to a step voltage command change 500V to 550V by various controllers. The effectiveness of VFFC and the VRECC in tracking response improvements can be observed.

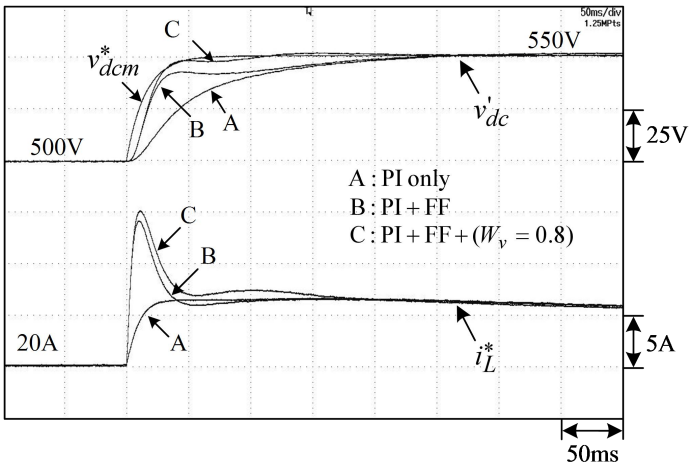

Figure 11 Measured $v_{dc}^{'}$ and i_L^* of the boost converter due to a step voltage command change 500V to 550V at $(V_{dc} = 500V, R_{dc} = 100\Omega)$ by various controllers.

Under the varied case $(V_{dc} = 500\text{V}, R_{dc} = 100\Omega)$, Figure 12 shows the measured $v_{dc}^{'}$ and i_L^* due to a step load resistance change of $R_{dc} = 100\Omega \rightarrow 93.75\Omega$ by various controllers. The results also demonstrate enhanced regulation responses in $v_{dc}^{'}$. The fast-tracking and regulation of DC-link voltage responses can enhance the EV SynRM driving performance.

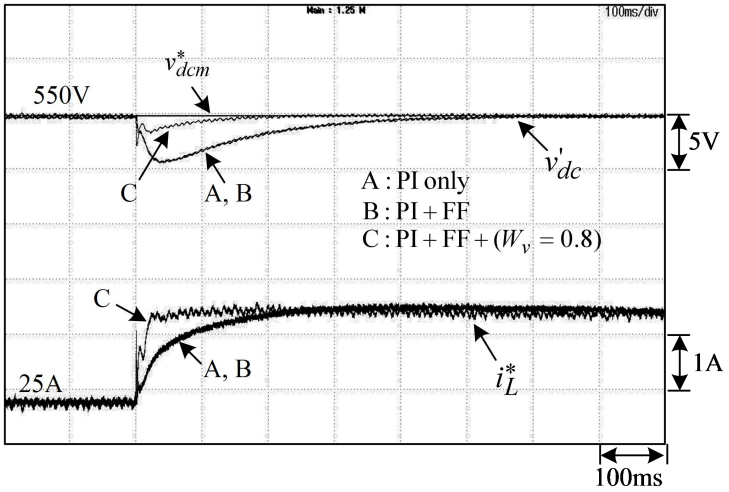

Figure 12 Measured v'_{dc} and i^*_L of the boost converter due to a step load resistance change $R_{dc} = 100\Omega \rightarrow 93.75\Omega$ at ($V_{dc} = 500\text{V}, R_{dc} = 100\Omega$) by various controllers.

5. Whole EV SynRM Drive Performance Evaluation

5.1 DC-link Voltage Setting

Generally, the EV is not operated at high speed in urban areas. Hence, for the battery-powered motor drive with DC/DC interface converter, the boosted DC-link voltage can vary with speed to reduce the total losses of the inverter-fed motor over a wide speed range. The proposed DC-link voltage versus speed profile is as follows:

$$v^*_{dc} = 160 + \frac{550–160}{2000}\omega^*_r(V) \#(21)$$

Here $0 \leq \omega^*_r \leq 2000\text{rpm}$.

5.2 Efficiency Assessment

The M-G set back-to-back approach is adopted here for making the test. For the load generator possessing nearly identical efficiency to the tested SynRM, the motor efficiency is estimated by assuming,

$$\eta_m \equiv \sqrt{\eta_{mg}},\ \ \eta_{mg} \equiv P_g/P_m \#(22)$$

Usually, the SPMSG is used, as the complicated commutation setting is non-essential for suitable generating capability. It is roughly reasonable for the high efficiencies of both the studied SynRM and the adopted load SPMSG. At four speeds and $R_L = 16.67\Omega$, under the cases of varied v_{dc} and $\beta = \beta_o$, the steady-state characteristics of the established EV SynRM drive are measured.

For verifying the correctness of the proposed commutation approach, the efficiencies of η_{mg} and η_m, manually set commutation angles at ($\omega_r = 2000\text{rpm}, V_{dc} = 550\text{V}, R_L = 16.67\Omega$), near rated load, are also measured. The maximum efficiency of $\eta_m = 0.9243$ at $\beta = 62.5°$ is obtained, which is closer to the one of $\eta_m = 0.923$ by the developed ACS with $\beta = \beta_o$, as indicated in Figure 13.

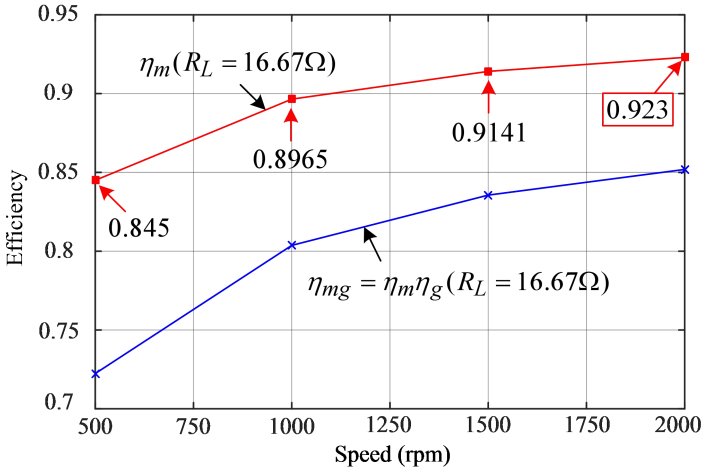

Figure 13 Measured efficiencies η_{mg} and $\eta_m \equiv \sqrt{\eta_{mg}}$ under various speeds for varied v_{dc} and $\beta = \beta_o$ at $R_L = 16.67\Omega$.

5.3 Energy Consumption Characteristics

Figure 14 shows the measured $(\omega_r^*, \omega_r^{'}), (v_{dc}^*, v_{dc}^{'}), v_b, i_b, P_b, E_b)$ for the established EV SynRM drive due to the ECE15 speed command pattern at $(\beta = \beta_o,\ R_L = 16.67\Omega)$ with varied DC-link voltage from $v_{dc} = 160\text{V}$ to 550V.

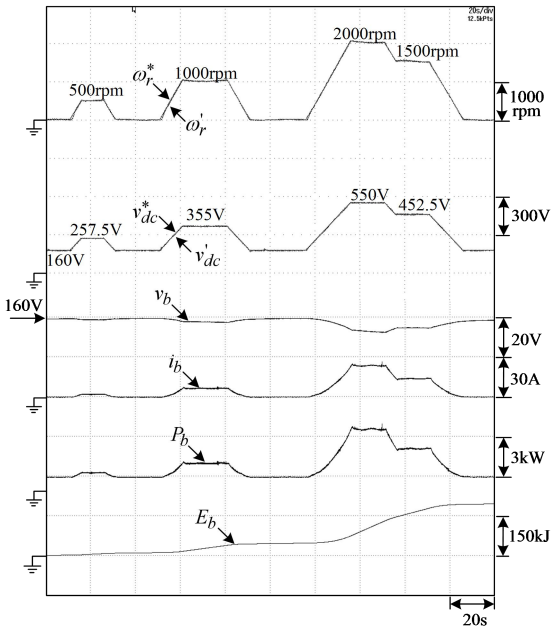

Figure 14 Measured $((\omega_r^*, \omega_r^{'}),(v_{dc}^*, v_{dc}^{'}), v_b, i_b, P_b, E_b)$ of the EV SynRM drive due to the speed pattern defined by ECE15 at $(\beta = \beta_o, R_L = 16.67\Omega)$ with varied DC-link voltage from 160V to 550V (0 to 2000 rpm).

Figure 15 compares the corresponding consumed battery energies $E_b \equiv \int P_b dt$ curves at $R_L = 16.67\Omega$ under four cases (fixed $v_{dc} = 550\text{V}$, $\beta = 45°$, fixed $v_{dc} = 550\text{V}$, $\beta = \beta_o$, varied v_{dc}, $\beta = 45°$, and varied $v_{dc}, \beta = \beta_o$). The results demonstrate normal speed tracking characteristics and reduced battery energy consumption by the developed commutation and the variable DC-link voltage approaches, as depicted in Figures 14 and 15.

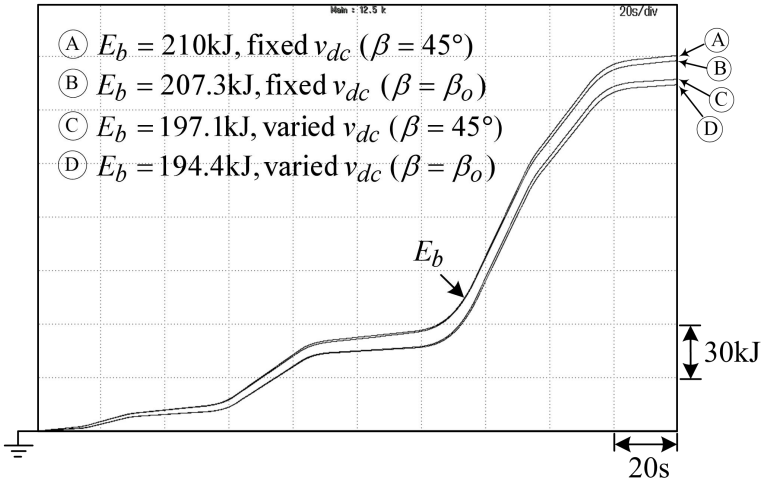

Figure 15 Measured E_b of the EV SynRM drive at $R_L =$ 16.67Ω with fixed $v_{dc} = 550$V and varied v_{dc}, $\beta = \beta_{o1} = 45°$ and $\beta = \beta_o$ due to the speed pattern defined by ECE15.

6. EV Grid-Connected Operations

6.1 Three-Phase SMR

For grid-connected operations, the EV SynRM drive is operated in idle mode by placing the switch SW in Figure 3 at position "2". The existing three-phase inverter is operated as a bilateral SMR with the addition of external LC low-pass filters.

6.1.1 Power Circuit

The specifications and the designed system parameters of the established three-phase SMR are as follows: (1) $V_{AB} = 220$V/60Hz; $V_{dc} = 550$V; (2) PWM switching frequency: $f_s = 20$ kHz; (3) Energy storage inductors: $L_A = L_B = L_C = 2.75$ mH (at 20 kHz); (4) Output filtering capacitor: $C_{dc} = 1100$ μF/800V.

6.1.2 Control Scheme

The designed PI controllers are as follows:

Current Controller. $G_{ci}(s) = 2.5 + 500/s$.

Voltage Controller. $G_{cv}(s) = 3.255 + 9.759/s$.

PLL Controller. $G_{pll}(s) = 20 + 80000/s$.

6.1.3 Grid-to-Vehicle Charging Operation

In G2V operation, the DC-link voltage is established from the utility grid through the three-phase inverter operated as an SMR. The DC/DC interface converter is operated in charging mode by positioning the switch in Figure 7(b) as SWB → Ⓑ. The battery voltage command is at $v_b^* = 170$V, and the battery charging current limit is 5A. Figures 16(a) and 16(b) show the measured (v_{dc}, v_b, i_L) and (v_A, i_A) of phase-A. The results demonstrate that the normal battery charging operation with good line-drawn power quality.

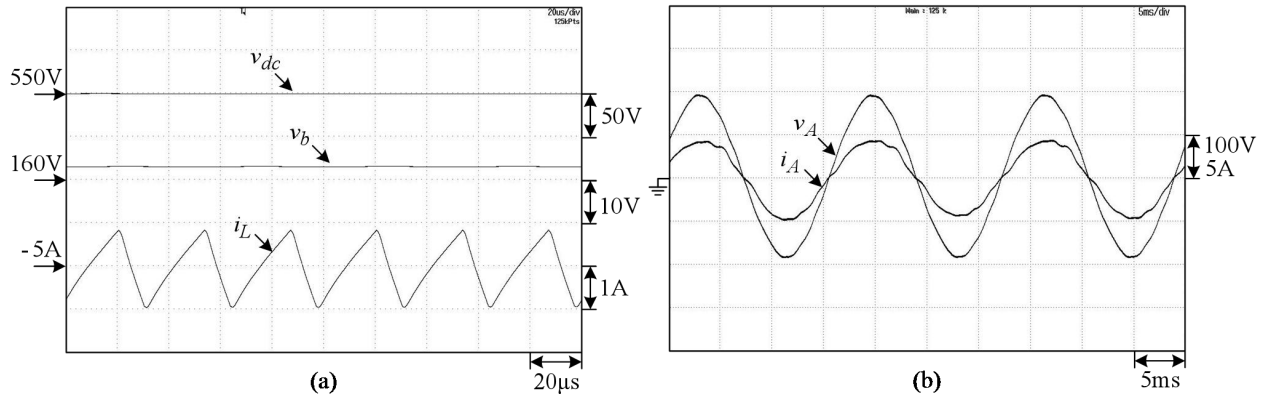

Figure 16 Measured results of the EV SynRM drive under G2V battery charging operation using three-phase SMR: (a) (v_{dc}, v_b, i_L); (b) (v_A, i_A).

6.1.4 Vehicle-to-Grid Discharging Operation

In V2G operation, the one-leg DC/DC converter is operated in discharging mode by positioning SWB at Ⓐ, and the power command P_b^* is set under power mode by positioning SWA to "2". The current command is given by the current command generator using the set power command P_b^* and the sensed battery voltage. Figure 17 shows the measured results at $P_b^* = 3000\text{W}$. Successful V2G operation can be seen from the reverse phase of i_A concerning v_A.

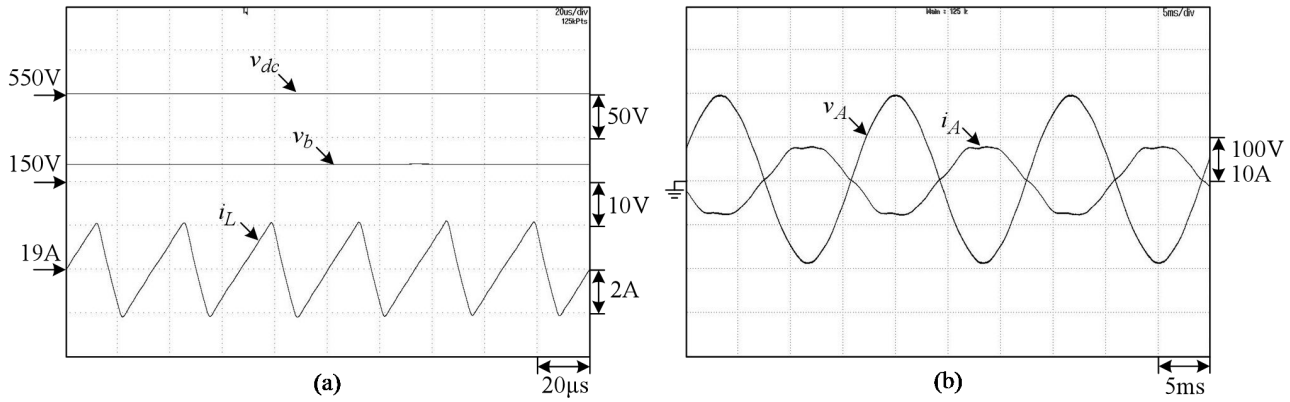

Figure 17 Measured results of the EV SynRM drive under V2G discharging operation using a three-phase inverter with $P_b^* = 3$ kW: (a) (v_{dc}, v_b, i_L); (b) (v_A, i_A).

6.2 Single-Phase SMR with External Inductor

6.2.1 Power Circuit

As shown in Figures 3 and 4(a), the single-phase H-bridge converter is constructed from the three-phase inverter with two legs $(L_A, L_B, T_1, T_4, T_3, T_6, C_{dc})$. The grid input source is AC 220V/60Hz. Figure 18 shows the control scheme of this SMR. Besides, the control scheme of the one-leg boost buck interface converter is identical to Figure 7(b).

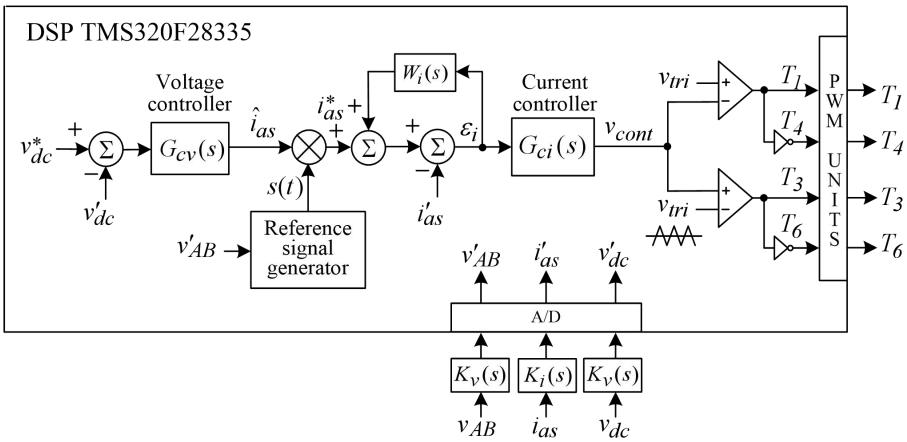

Figure 18 Control scheme of the single-phase H-bridge SMR.

The specifications and system variables of the designed SMR are: (1) $V_{AB} = 220\text{V}/60\text{Hz}$; (2) $V_{dc} = 550\text{V}$, $P_{dc} = 1.5\text{ kW}$; (3) Output filtering inductor $L = L_A + L_B = 5.5\text{ mH}$; (4) Output filtering capacitor: $C_o = 3.3\ \mu\text{F}/400\text{V}$; (5) $C_{dc} = 1100\ \mu\text{F}/800\text{V}$.

6.2.2 Control Scheme

The chosen controllers are as follows:

Current Feedback and Robust Controllers.

$$G_{ci}(s) = 3 + \frac{1600s}{s^2 + 80s + 377^2} \#(23)$$

$$W_i(s) = \frac{W_i}{1 + \tau_i s} = \frac{0.6}{1 + 5.31 \times 10^{-5} s} \#(24)$$

Voltage Controller.

$$G_{cv}(s) = K_{Pv} + \frac{K_{Iv}}{s} = 1 + \frac{50}{s} \#(25)$$

6.2.3 Grid-to-Vehicle Charging Operation

The constant current charging command is limited to 3A. Figures 19(a) and 19(b) show the measured (v_{AB}, i_A), $(i_{as}^*, i_{as}^{'})$ of the SMR, and (v_{dc}, v_b, i_L) of the one-leg converter-based charger and normal G2V charging operation can also be observed.

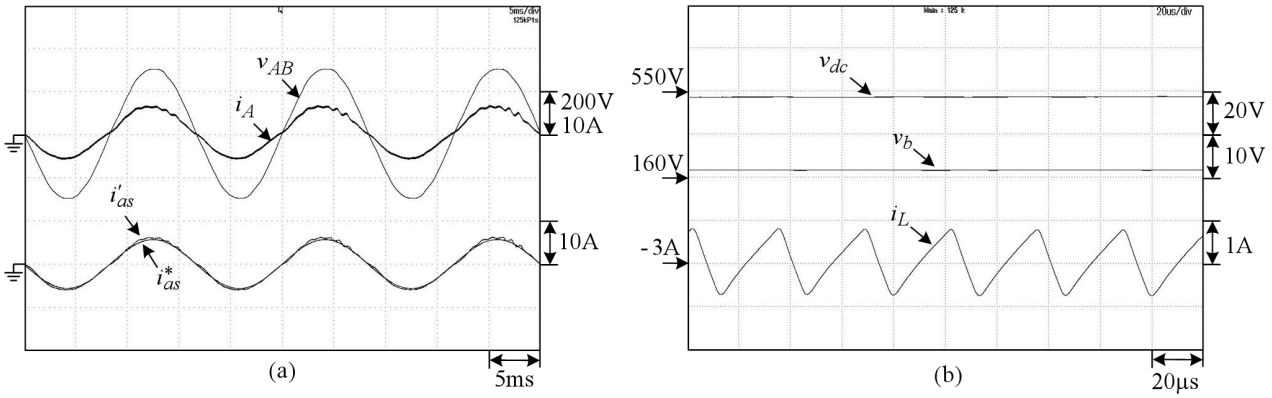

Figure 19 Measured results of the EV SynRM drive under G2V charging operation with single-phase SMR: (a) (v_{AB}, i_A), (i^*_{as}, i'_{as}); (b) (v_{dc}, v_b, i_L).

6.2.4 Vehicle-to-Grid Discharging Operation

Figures 20(a) and 20(b) depicts the measured $((v_{AB}, i_A), (i^*_{as}, i'_{as}))$ of the SMR and (v_{dc}, v_b, i_L) of the one-leg converter by setting $P^*_b = 1.5$ kW. The successful V2G operation is apparent from the results.

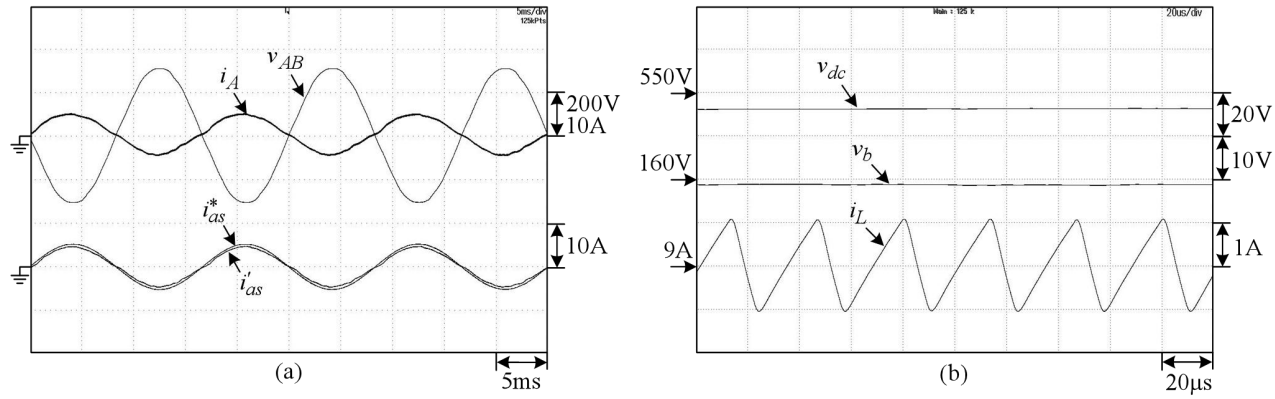

Figure 20 Measured results of the EV SynRM drive under V2G discharging operation with single-phase SMR: (a) (v_{AB}, i_A), (i^*_{as}, i'_{as}); (b) (v_{dc}, v_b, i_L).

6.3 Single-phase SMR with Integrated Inductor

6.3.1 Power Circuit

Figure 4(b) depicts the developed EV SynRM drive in single-phase G2V/V2G modes using an integrated inductor. The two serially connected armature windings serve as the energy storage inductor for the SMR and the output filtering inductor for the inverter. Figure 21 shows the measured inductance profiles L_{ab} using LCR meter at two frequencies. The maximum inductance directed under the d-axis at 20 kHz is $L_{ab,\max} = 42.97\text{mH}$ higher than the externally added $L = L_A + L_B = 5.5\text{mH}$. In actual operation, the rotor of SynRM is naturally locked at this position with $L_{ab} = 42.97\text{mH}$.

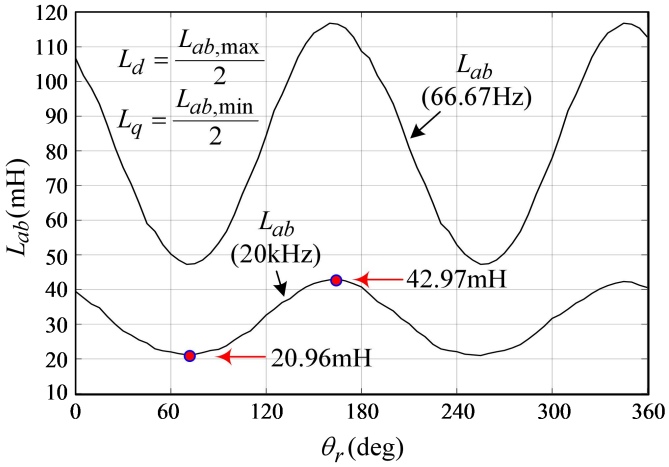

Figure 21 Measured inductance profiles L_{ab} of the employed SynRM at two frequencies.

6.3.2 Control Scheme

The control scheme is the same as Figure 18. As the adopted laminated winding inductor has different characteristics than the ferrite core inductor, the PR current feedback controller is slightly modified as,

$$G_{ci}(s) = 8 + \frac{1600s}{s^2 + 80s + 377^2} \#(26)$$

6.3.3 Grid-to-Vehicle Charging Operation

Under the constant current charging command of 3A, ($(v_{AB}, i_A), (i_{as}^*, i_{as}^{'})$) of the SMR and (v_{dc}, v_b, i_L) of the one-leg converter are measured (Figures 22(a) and 22(b)). The results demonstrate normal operation.

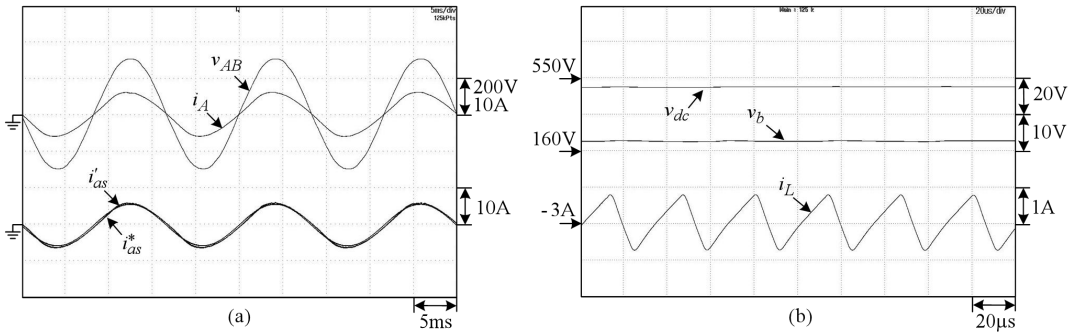

Figure 22 Measured results of the EV SynRM drive under G2V charging operation with single-phase SMR using integrated inductor of armature windings: (a) $(v_{AB}, i_A), (i_{as}^*, i_{as}^{'})$; (b) (v_{dc}, v_b, i_L).

6.3.4 Vehicle-to-grid Discharging Operation

Figures 23(a) and 23(b) show plots of the measured ($(v_{AB}, i_A), (i_{as}^*, i_{as}^{'})$) of the SMR using an integrated inductor and (v_{dc}, v_b, i_L) of the one-leg converter by setting the power command $P_b^* =$

1.5kW. The results indicate the successful V2G operation, confirmed by the 180° phase difference between v_{AB} and i_A.

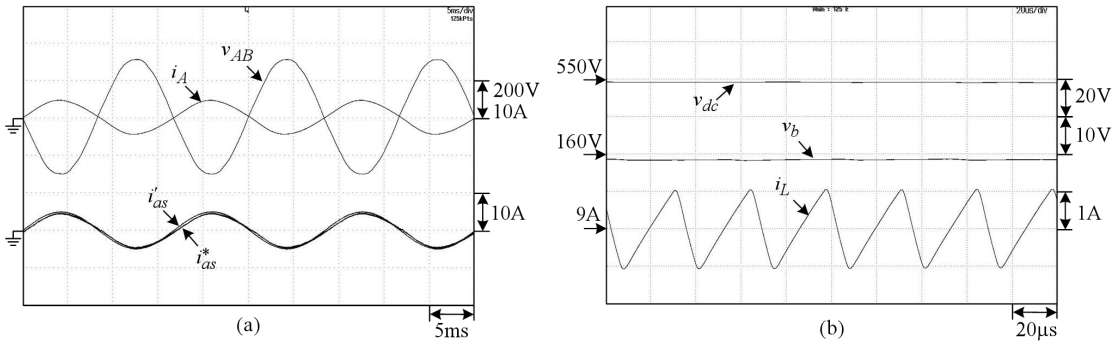

Figure 23 Measured results of the EV SynRM drive under V2G discharging operation with single-phase SMR using integrated inductor of armature windings: (a) (v_{AB}, i_A), (i^*_{as}, i'_{as}); (b) (v_{dc}, v_b, i_L).

Comparing Figure 22 to Figure 19 and Figure 23 to Figure 20 reveals that the resulted current waveforms using integrated inductors are less distorted than the externally added ones. The quantitative comparisons of power qualities and efficiencies of the single-phase G2V/V2G operations using the SMRs with two types of inductors are as follows:

G2V comparison

Parameters	Externally added inductors	Integrated inductors
THDi	5.98%	3.08%
PF	0.9843	0.9909
$\eta = P_b/P_{ac}$	78.34%	76.88%

V2G comparison

Parameters	Externally added inductors	Integrated inductors
THDi	5.28%	4.01%
PF	0.9917	0.9927
$\eta = P_b/P_{ac}$	83.91%	80.49%

The results demonstrate that using armature winding laminated core inductor yields slightly better performance in current THD and power factor, but the efficiencies are slightly low.

7. EV and Microgrid Interconnected Operations

As shown in Figure 3, the bidirectional M2V/V2M operations can be performed by connecting the DC-link of EV to the microgrid DC-bus. Figure 24(a) shows the studied wind SRG based DC microgrid. The asymmetric bridge converter is applied to the SRG for the best control flexibility.

The SRG control scheme considering proper commutation shift can be referred to in an earlier study [35]. Table 1 enlists some main parameters of the redesigned wind SRG based DC microgrid.

Table 1 Some key parameters of the established wind SRG based DC microgrid.

SRG and interface converter	
Parameters	Values
Rated speed	6000rpm
Rated power	2.3 kW
Rated voltage	48V
Mechanic	4-phase, 8/6 teeth
Energy storage inductor L_1	862.7 μF
Filtering capacitor C_d	51700 μF/100V
DC-bus capacitor C_{dc2}	2200 μF/450V
Switching frequency f_s	30 kHz
Battery energy storage system	
Parameters	Values
Rated voltage and capacity	48V (12V×4, 36Ah)
Energy storage inductor L_{b2}	308.507 μH
Filtering capacitor C_{b2}	2200 μF/450V
Switching frequency f_s	30 kHz

The control schemes of the interface converters of the SRG and the battery energy storage system are shown in Figure 24(b). Power-sharing can avoid a shortage of wind power. As per the speed-dependent back-EMF of the employed SRG, the generated voltage commands are set as 6000rpm >> 48V; 5000rpm >> 42V and 4000rpm >> 36V.

For the load 1P3W inverter, the outer legs produce the 220V/60Hz line-to-line voltage, while the central leg balances the two phase-to-neutral 110V/60Hz voltages. The output filters are designed as $C_o = 10\ \mu\text{F}$, $L_{o1} = 2.048\text{mH}/60\text{Hz}$, $L_{o2} = 2.093\text{mH}/60\text{Hz}$, $L_{o3} = 2.102\text{mH}/60\text{Hz}$. The low-pass cut-off frequency for v_{AB} is $f_c = \frac{1}{2\pi\sqrt{0.5(L_{o1}+L_{o3})\,C_o}} = 1104.87\text{Hz}$. For the test loads, the incandescent lamps of $Z_A = Z_B = 115V/100\text{W}$, $Z_{AB} = 220V/100\text{W}$ are used. For the control scheme shown in Figure 24(c), the proportional-resonant (PR) controllers are applied to both voltage and current loops for yielding better sine-wave tracking control.

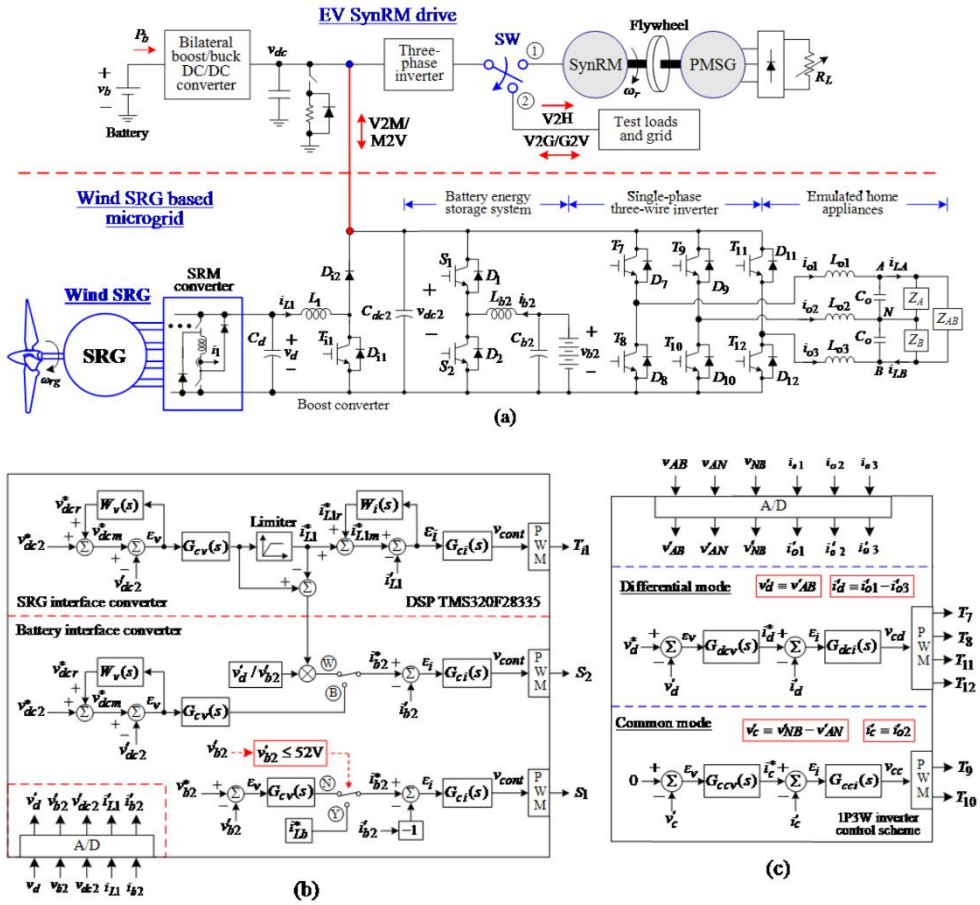

Figure 24 The established wind SRG based microgrid: (a) Power circuit; (b) Control schemes of SRG and battery interface converters; (c) Control scheme of 1P3W load inverter.

7.1 Microgrid-to-vehicle Operation

7.1.1 Sufficient Wind Power

Assuming adequate wind power and the wind SRG between 6000 rpm and 5000 rpm, Figures 25(a) and 25(b) show the measured results under M2V operation at the preset constant EV battery charging $i_b^* = -3\text{A}$. Figures 26(a) and 26(b) shows the measured steady-state waveforms, where normal operations of all constituted power stages are observed. The SRG output voltages are quickly and stably regulated at set $V_d = 48\text{V}$ and 42V, while the well-regulated common DC-bus voltage $V_{dc2} = 400\text{V}$ is established through the interface converter. The smooth EV battery charging can also be observed.

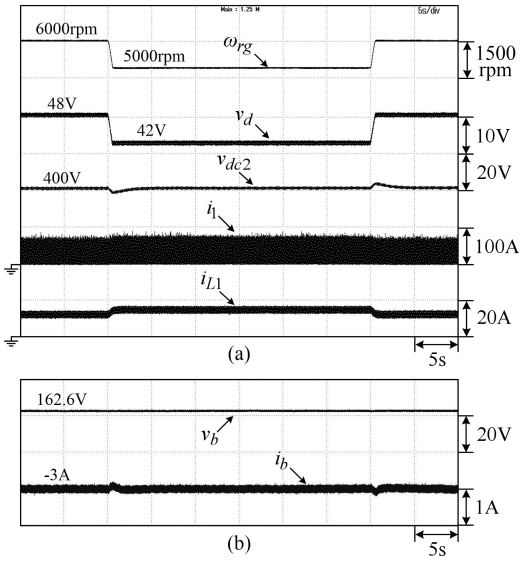

Figure 25 M2V operation under constant EV battery charging $i_b^* = -3A$ with enough wind power: (a) SRG key waveforms; (b) EV battery.

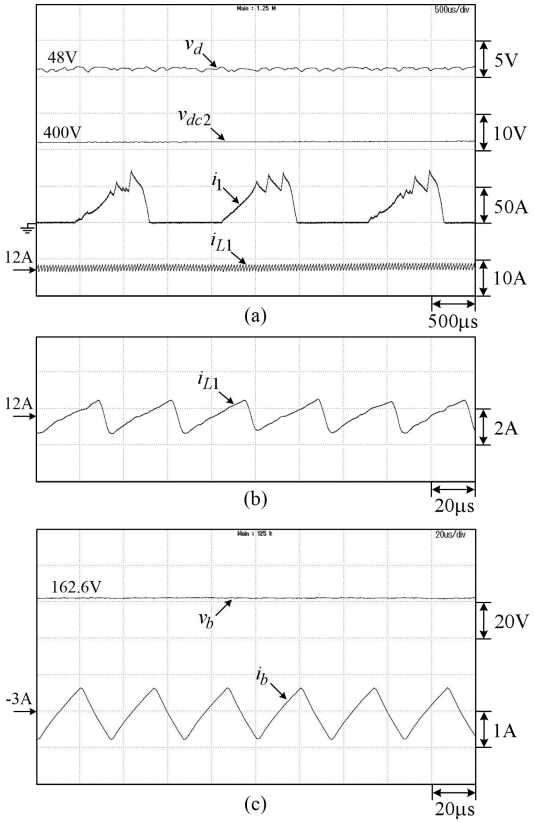

Figure 26 Steady-state waveforms corresponding to Figure 25 at 6000 rpm: (a) $(v_d, v_{dc2}, i_1, i_{L1})$; (b) Magnified i_{L1}; (c) (v_b, i_b)

7.1.2 Insufficient Wind Power

A current limit of 13A is set to the SRG interface converter to emulate the occasion of insufficient wind power, as shown in Figure 24(b). As the wind speed is reduced with less

generated power to let the current command reach the preset limit, the remaining load power will automatically be supported by the battery energy storage system.

Figures 27(a) to 27(c) show the measured results of M2V operation considering insufficient wind power. The load is arranged to be the EV battery under constant current charging with $i_b^* = -3\text{A}$. The wind SRG driven speeds are set as 6000 rpm >> 5000 rpm >> 4000 rpm. As the speed changes from 5000 rpm to 4000 rpm, the current command reaches the current limit. Henceforth, the battery energy storage system starts to support the remaining demand. Figures 25 and 27 demonstrate that M2V operation can be successfully conducted by the established DC microgrid and EV SynRM drive.

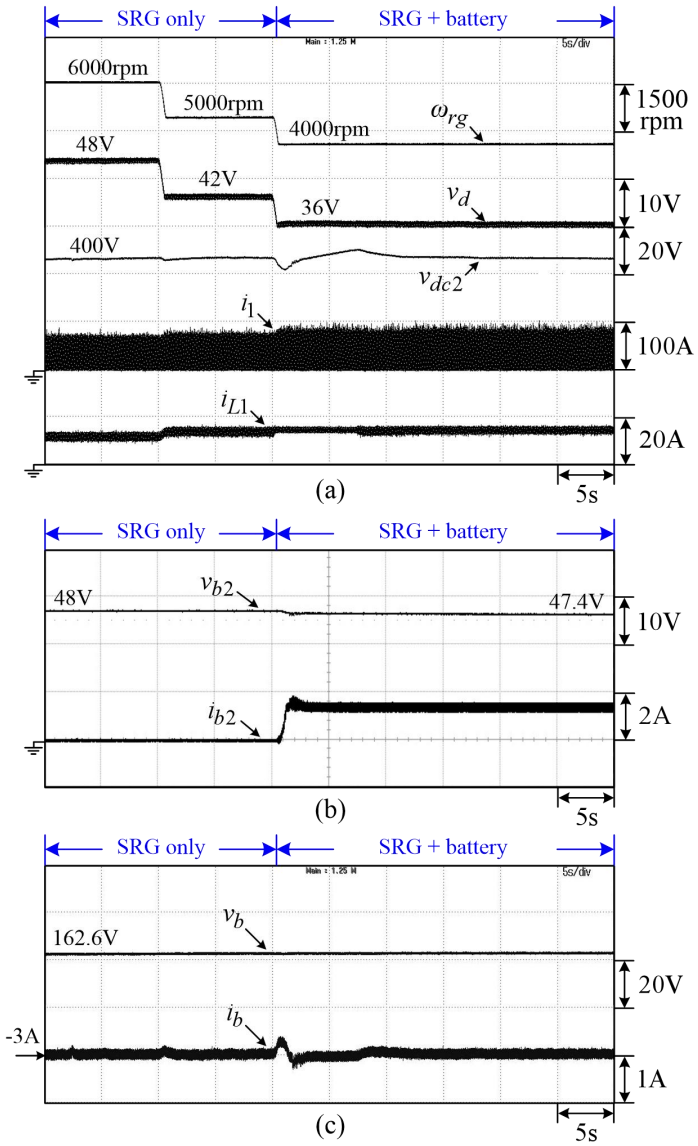

Figure 27 Measured results of M2V operation with EV battery constant current charging ($i_b^* = -3A$) considering insufficient wind power: (a) SRG key waveforms; (b) Battery energy storage system; (c) EV battery.

7.2 Vehicle-to-Microgrid Operation

In V2M discharging operation, the microgrid DC link voltage $v_{dc2} = 400\text{V}$ is established by the EV battery. Figures 28(a) to 28(c) present plots for the measured (v_b, v_{dc2}, i_b) of EV SynRM drive, (v_{AN}, v_{NB}, i_{LA}) and (v_{AB}, i_{LA}) of microgrid 1P3W inverter, under the arranged test loads. The results illustrate the output line-to-line and balanced phase-to-neutral voltages with good waveform quality.

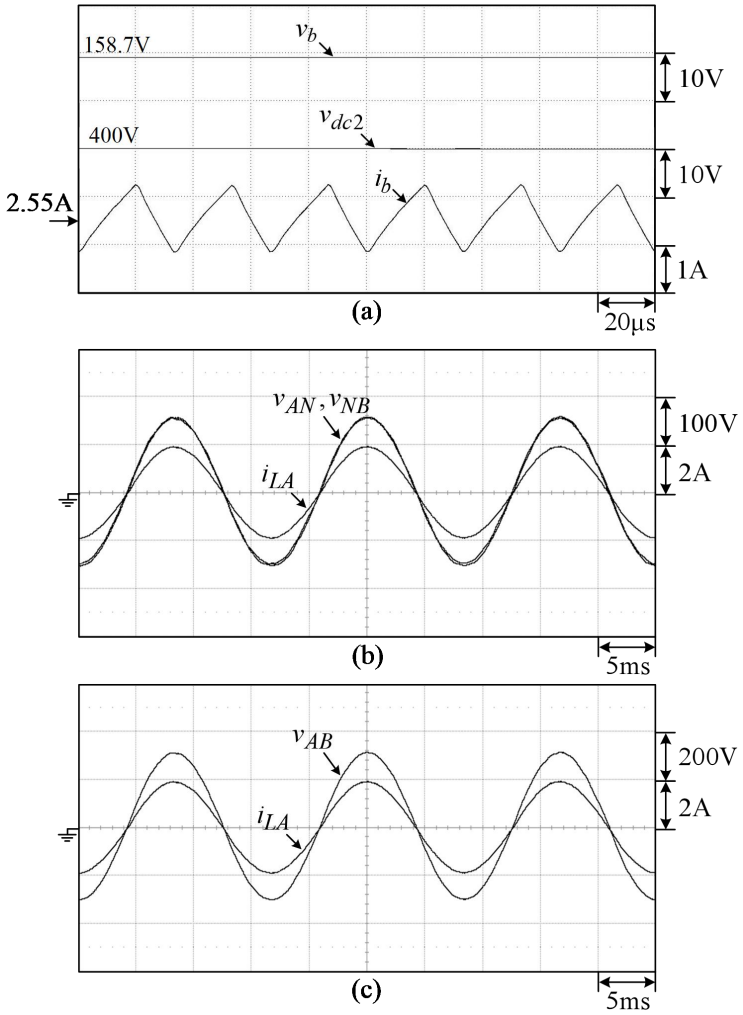

Figure 28 Measured results V2M operation: (a) (v_b, v_{dc2}, i_b) of EV SynRM drive; (b) (v_{AN}, v_{NB}, i_{LA}) of microgrid 1P3W inverter; (c) (v_{AB}, i_{LA}) of microgrid 1P3W inverter.

8. Conclusions

This study has developed an EV SynRM drive and the G2V/V2G and M2V/V2M operations. First, the SynRM drive is established. The highly efficient operating performance is achieved by the adaptive commutation angle with loss minimization and robust current control considering slotting effects. Later, the proper designs for the coordinated outer motor drive speed loop and battery-interface converter voltage loop are made. The proposed speed varied DC-link voltage yields improved motor efficiency and battery energy consumption over a wide speed range. The measured results showed that the SynRM efficiency reaches 92.3% near the rated load.

In the idle mode, the EV drive three-phase inverter is arranged to be a bidirectional SMR. Further, in G2V mode, the on-board battery is charged from the utility grid with good line-drawn power quality. Conversely, in V2G mode, the power is sent back to the utility grid with good line current waveform quality. In single-phase cases, the integrated inductor using armature windings is also conducted and comparatively evaluated.

For M2V/V2M operations, the EV drive is interfaced to a wind SRG based DC microgrid. The measured results of M2V operation show superior EV on-board battery charging characteristics. In V2M mode, the EV battery can power the microgrid home appliances with well-regulated 220V/110V 60Hz AC voltages and good waveform qualities. The measured results verify the normal operations and satisfactory performances for all the established power stages under various operation cases.

Author Contributions

Ganisetti Vijay Kumar: Main author involving the measurements and the paper writing; Min-Ze Lu: Assisting the author and doing the proofreading; Chang-Ming Liaw: Advisor giving suggesting and doing the proofreading.

Competing Interests

The authors have declared that no competing interests exist.

References

1. Miller TJ, Hutton A, Cossar C, Staton DA. Design of a synchronous reluctance motor drive. IEEE Trans Ind Appl. 1991; 27: 741-749.
2. Krause P, Wasynczuk O, Sudhoff SD, Pekarek SD. Analysis of electric machinery and drive systems. 3rd ed. Hoboken, New Jersey: John Wiley & Sons; 2013.
3. Ferrari M, Bianchi N, Doria A, Fornasiero E. Design of synchronous reluctance motor for hybrid electric vehicles. IEEE Trans Ind Appl. 2015; 51: 3030-3040.
4. Bianchi N, Bolognani S, Carraro E, Castiello M, Fornasiero E. Electric vehicle traction based on synchronous reluctance motors. IEEE Trans Ind Appl. 2016; 52: 4762-4769.
5. Trancho E, Ibarra E, Arias A, Kortabarria I, Jurgens J, Marengo L, et al. PM-assisted synchronous reluctance machine flux weakening control for EV and HEV applications. IEEE Trans Ind Electron. 2018; 62: 2986-2995.
6. Qu ZC, Hinkkanen M. Loss-minimizing control of synchronous reluctance motors - A review. Proceeding of IEEE International Conference on Industrial Technology; 2013 February 23-25; Cape Town, South Africa.
7. Hofmann HF, Sanders SR, EL-Antably A. Stator-flux- oriented vector control of synchronous reluctance machines with maximized efficiency. IEEE Trans Ind Electron. 2004; 51: 1066-1072.
8. Inoue Y, Morimoto S, Sanada M. A novel control scheme for maximum power operation of synchronous reluctance motors including maximum torque per flux control. IEEE Trans Ind Appl. 2011; 47: 115-121.
9. Yamamoto S, Hirahara H, Adawey JB, Ara T, Matsuse K. Maximum efficiency drives of synchronous reluctance motors by novel loss minimization controller with inductance estimator. IEEE Trans Ind Appl. 2013; 49: 2543-2551.

10. Bedetti N, Calligaro S, Petrella R. Self-adaptation of MTPA tracking controller for IPMSM and SynRM drives based on on-line estimation of loop gain. Proceeding of the IEEE Energy Conversion Congress and Exposition; 2017 October 1-5; Cincinnati, OH, USA.
11. Vijay Kumar G, Chuang CH, Lu MZ, Liaw CM. Development of an electric vehicle synchronous reluctance motor drive. IEEE Trans Veh Technol. 2020; 69: 5012-5024.
12. Mahmoud H, Bianchi N. Nonlinear analytical model of eccentric synchronous reluctance machines considering the iron saturation and slotting effect. IEEE Trans Ind Appl. 2017; 53: 2007-2015.
13. Antonello R, Ortombina L, Tinazzi F, Zigliotto M. Advanced current control of synchronous reluctance motors. Proceeding of the IEEE 12th International Conference on Power Electronics and Drive Systems; 2017 December 12-15; Honolulu, HI, USA.
14. Wiedemann S, Kennel RM, Hall S, Alakula M. Dynamic testing characterization of a synchronous reluctance machine. IEEE Trans Ind Appl. 2018; 54: 1370-1378.
15. Schoenen T, Kunter MS, Hennen MD, De Doncker RW. Advantages of a variable DC-link voltage by using a DC-DC converter in hybrid electric vehicles. Proceeding of the IEEE Vehicle Power and Propulsion Conference; 2010 September 1-3; Lille, France.
16. Estima JO, Marques Cardoso AJ. Efficiency analysis of drive train topologies applied to electric/hybrid vehicles. IEEE Trans Veh Technol. 2012; 61: 1021-1031.
17. Khan MA, Ahmed A, Hussain I, Sozer Y, Badawy M. Performance analysis of bidirectional DC-DC converters for electric vehicles. IEEE Trans Ind Appl. 2015; 51: 3442-3452.
18. Prabhakar KK, Ramesh M, Dalal A, Reddy CU, Singh AK, Kumar P. Efficiency investigation for electric vehicle powertrain with variable DC-link bus voltage. Proceeding of the 42nd Annual Conference of the IEEE Industrial Electronics Society; 2016 October 23-26; Florence, Italy.
19. Bhattacharjee A, Mohanty RK, Ghosh A. Design of an optimized thermal management system for Li-ion batteries under different discharging conditions. Energies. 2020; 13: 5695.
20. Pinto JG, Monteiro V, Gonçalves H, Exposto B, Pedrosa D, Couto C, et al. Bidirectional battery charger with grid-to-vehicle, vehicle-to-grid and vehicle-to-home technologies. Proceeding of the 39th Annual Conference of the IEEE Industrial Electronics Society; 2013 November 10-13; Vienna, Austria.
21. Kramer B, Chakraborty S, Kroposki B. A review of plug-in vehicles and vehicle-to-grid capability. Proceeding of the 34th Annual Conference of IEEE Industrial Electronics; 2008 November 10-13; Orlando, FL, USA.
22. Kramer W, Chakraborty S, Kroposki B, Hoke A, Martin G, Markel T. Grid interconnection and performance testing procedures for vehicle-to-grid (V2G) power electronics. Tech Rep NREL; 2012: 1-8.
23. Haghbin S, Lundmark S, Alaküla M, Carlson O. Grid-connected integrated battery chargers in vehicle applications: Review and new solution. IEEE Trans Ind Electron. 2013; 60: 459-473.
24. Ustun TS, Ozansoy CR, Zayegh A. Implementing vehicle-to-grid (V2G) technology with IEC 61850-7-420. IEEE Trans Smart Grid. 2013; 4: 1180-1187.
25. Liu CH, Chau KT, Wu DY, Gao S. Opportunities and challenges of vehicle-to-home, vehicle-to-vehicle, and vehicle-to- grid technologies. Proc IEEE Inst Electr Electron Eng. 2013; 101: 2409-2427.
26. Hu KW, Liaw CM. Incorporated operation control of DC microgrid and electric vehicle. IEEE Trans Ind Electron. 2016; 63: 202-215.

27. Masrur MA, Skowronska AG, Hancock J, Kolhoff SW, McGrew DZ, Vandiver JC, et al. Military-based vehicle-to-grid and vehicle-to-vehicle microgrid-system architecture and implementation. IEEE Trans Transport Electrific. 2018; 4: 157-171.
28. Das D, Weise N, Basu K, Baranwal R, Mohan N. A bidirectional soft-switched DAB-based single-stage three-phase AC-DC converter for V2G application. IEEE Trans Transport Electrific. 2019; 5: 186-199.
29. Khaligh A, Antonio MD. Global trends in high-power on-board chargers for electric vehicles. IEEE Trans Veh Technol. 2019; 68: 3306-3324.
30. Chandra Mouli GR, Schijffelen J, van den Heuvel M, Kardolus M, Bauer P. A 10 kW solar-powered bidirectional EV charger compatible with Chademo and COMBO. IEEE Trans Power Electron. 2019; 34: 1082-1098.
31. Rahman MS, Hossain MJ, Lu JW. Utilization of parked EV-ESS for power management in a grid-tied hybrid ac/dc microgrid. Proceeding of the IEEE Australasian Universities Power Engineering Conference; 2015 September 27-30; Wollongong, NSW, Australia.
32. Dicorato M, Forte G, Trovato M, Muñoz CB, Coppola G. An integrated DC microgrid solution for electric vehicle fleet management. IEEE Trans Ind Appl. 2019; 55: 7347-7355.
33. Mehrjerdi H, Hemmati R. Electric vehicle charging station with multilevel charging infrastructure and hybrid solar-battery-diesel generation incorporating comfort of drivers. J Energy Storage. 2019; 26: 100924.
34. Mehrjerdi H, Hemmati R. Stochastic model for electric vehicle charging station integrated with wind energy. Sustain Energy Technol Assess. 2020; 37: 100577.
35. Mehrjerdi H, Hemmati R. Coordination of vehicle-to-home and renewable capacity resources for energy management in resilience and self-healing building. Renew Energy. 2020; 146: 568-579.
36. Chang YC, Liaw CM. On the design of power circuit and control scheme for switched reluctance generator. IEEE Trans Power Electron. 2008; 23: 445-454.
37. Ghosh A. Possibilities and challenges for the inclusion of the electric vehicle (EV) to reduce the carbon footprint in the transport sector: A review. Energies. 2020; 13: 2602.